Molecular scale insight of pore morphology relation with mechanical properties of amorphous silica using ReaxFF

Truong Vo[a], Bang He[a], Michael Blum[a,b], Angelo Damone[c], Pania Newell[a,*]

[a]*Department of Mechanical Engineering, the University of Utah, Salt Lake City, UT 84112, USA*
[b]*School of Computing, the University of Utah, Salt Lake City, UT 84112, USA*
[c]*Department of Mechanical Engineering, University of Brescia, Brescia 25123, Italy*

Abstract

Porous materials are typically heterogeneous and they contain large variations of micro-/nano-pore structures, causing complicated behaviors. In continuum models, most mechanical properties of porous materials are estimated based on porosity, while the variations of micro/nano structures are ignored. That could be problematic as the microscopic heterogeneity may affect the mechanical response of porous materials. Thus, understanding micro/nano heterogeneity impact has been the focus in many scientific and engineering subjects. In the present study, we investigated the effect of nanopore structure (including pore shape and orientation) as well as porosity on mechanical properties of amorphous silica (a-SiO$_2$). The pore sizes in our simulations are comparable to the corresponding ones observed in a-SiO$_2$ based materials. We found that the existing of nanopores strongly influences Young's modulus (E) and critical energy release rate (G_{IC}). These properties decrease with increasing porosity. Importantly, the impact of nanopores was characterized by structural parameters of porous materials. In addition to dependency on porosity, Young's modulus also was found to vary as a function of potential energy per atom, which highly depends on nanopore shape. Furthermore, critical energy release rate was found to increase with increasing ligament length (also known as pore wall thickness). The results highlighted the importance of nanopore structures, which must be taken into account when studying fracture mechanisms in porous materials. Based on our findings, it was proposed that

---

*Corresponding author
Email address: Pania.Newell@utah.edu (Pania Newell)

mechanical properties of porous materials can be controlled by nano-engineering pore structures.

Highlights

- ReaxFF molecular dynamics were used to study mechanical properties of amorphous silica.

- Effect of porosity, pore shape and orientation was systematically investigated.

- Impact of nanopore structures were universally characterized.

- Mechanical properties can be controlled by nano-engineering pore structure.

---

1. Introduction

Porous media and porous materials containing pores or voids are surrounding the world around us in various forms [1]. For instance, natural porous materials are found in various geological and biological materials [2, 3]. Because of superior mechanical and thermal behaviors of natural porous materials, many man-made materials are also cast as porous materials [4] and are applied in all engineering and scientific fields (e.g., civil, mechanical, chemical engineering, etc.) [5, 6, 7, 8, 9]. However, the presence of pores complicates the behavior of porous materials, as the underlying pore structures (e.g. porosity, pore shape, pore size, and pore distribution) fundamentally affect the material's overall performance [10, 11]. These effects tend to be even more complex for multiphysics scenarios. Thus, understanding pore structures has been the focus in many science and engineering subjects [12, 13].

In the past several decades, a large number of research, particularly theoretical studies, have characterized and quantified properties and behaviors of various porous materials by considering their pore structures [14, 15]. Among these theoretical works, porosity, defined as the void-to-total volume fraction, is usually used as a principal quantity to connect pore structure and continuum behavior of

these porous materials [16]. Mechanical properties in some porous materials can be predicted based on pore structures and skeleton properties. From this perspective, a set of corresponding experimental and numerical research has illustrated that mechanical properties are closely related to porosity of porous media, particularly the overall stiffness [17, 18, 19, 20]. However, by just considering porosity, the variation of pore shape, pore size, and pore distribution will be ignored. One of the reasons for only considering porosity is that quantifying the micropore structure at continuum level is a challenging task.

In general, most porous materials are heterogeneous by nature. By using advanced imagining techniques, including neutron and X-ray scattering and X-ray or electron imaging, it has been determined that many porous materials exhibit a pore size distribution over many orders of magnitude, from 10^{-3} to 10^4 μm [12]. Several studies demonstrated that macroscopic properties are influenced by micro-/nano-pore structure [21, 22]. They showed that for the same porosity, micro pore orientation and shape highly influence the mechanical performance of materials. It was found that the strength of porous Ti35Nb4Sn alloy increases with higher aspect ratios of pore geometry [17]. Such ratios are very challenging to obtain as advanced imagining techniques with high resolution (e.g. 3D volumetric reconstruction) are required. Moreover, under a given porosity, Young's modulus, tensile strength, and hardness of nanoporous gold significantly change with the variation in the average ligament thickness (thickness of the pore walls) [18, 19]. Due to the complex topology of pore structures, and nonuniform statistical distributions of ligament sizes and interfaces, it is challenging to determine an accurate average ligament thickness. This challenge has led to inconsistency in defining the relationship between Young's modulus and ligament size of nanoporous gold as reported in the literature [20]. From the literature review given above, it is evident that there is a need to investigate the impact of micro-/nano-pore structure on the behavior of porous materials.

Due to the intrinsic microscale challenges, applying conventional continuum theory or experimental approach in this study may be cumbersome. Fortunately, new numerical methods (e.g. multi scale homogenization method [23]) provide a valuable opportunity to look into these problems. Recent studies also illustrate the significant advantage of numerical approaches in studying heterogeneous porous media [24, 25]. For example, numerical homogenization techniques can successfully extract homogenized material properties (e.g. stiffness, permeability) to characterize heterogeneous porous media. Recently, a two-scale homogenization-

3

based scheme was developed to examine the effect of micro-heterogeneity on fracture behavior in heterogeneous porous materials [26]. The results in that paper demonstrated that micropore shape not only affects fracture strength but also fracture propagation patterns. However, this numerical scheme is limited to evaluate homogenized stiffness based on the heterogeneous micros pore structure with periodic heterogeneity as required by the two-scale homogenization techniques [27, 28]. The complex material properties, such as energy release rate, still cannot be extracted from two-scale homogenization. Other studies have intergrated statistical tools with a numerical approach to model complex porous behaviors [26]; however, such studies do not account for heterogeneity in pore structure.

To address the limitations of the current studies, atomic-level simulation, such as molecular dynamics (MD), might be beneficial in deriving material properties in heterogeneous porous materials as they provide opportunities to examine complex material properties with intricate heterogeneity. Subsequently, one can implement the mechanical properties derived from atomic simulation to continuum level to establish a robust numerical model. For example, a combined MD and phase-field method has been published in a few recent articles [29, 30, 31]. It is noteworthy that the pivotal step in this approach is the quantification of the material properties based on atomic simulations. Thus, examining the pore structure impact offered through this study can significantly assist numerical modeling of porous media across scales.

In MD simulations, the atoms and the distance between them are governed by fundamental theories of chemistry. As a result, MD simulations provide a higher temporal and spatial resolution compared to continuum approaches, and is eligible to model a set of complex material properties and phenomena [32, 33, 34, 35]. There have been great efforts in understanding mechanical properties at the atomic level as summarized in a few review articles [36, 37, 38]. Currently, among published MD articles, crack propagation has been received the highest attention, while the role of nanopore structures has not been fully addressed yet. For instance, Priezjev et al. [39] studied porous glasses under steady shear. However, as the pore structures are formed randomly via a thermal quench process, the dependency of pore shape and orientation on mechanical properties has not been addressed. Winter et al. [40] investigated the effect of pore structure on the mechanical properties of nanoporous silicon. They found that the material stiffness strongly depends on porosity. They also studied the effect of porosity under various pore shapes and orientations. In another report, deformation behavior of

4

nanoporous $Cu_{64}Zr_{36}$ glass was examined under the influence of pore density, distribution, and size, where only circular pore shape was considered. In thoses published articles [40, 41], a quantification of the impact of pore structure remains unknown.

In this study, we investigate the effect of nanopore structures (including pore shape and pore orientation) on the mechanical properties of amorphous silica (a-SiO_2) using MD simulations. Porous a-SiO_2 is chosen as it has been considered a fascinating material for many technological applications due to its porous and morphological characteristics [42, 43]. Even though there have been several MD studies on the mechanical properties of a-SiO_2 investigating the effects of surface cracks [44, 45, 46], loading conditions [47], loading rate [48], and solid-fluid interactions [49, 50, 51], the role of nanopores on such properties has not been explored in these studies.

The remaining part of the paper is organized as follows. In section 2, we provide details about the numerical approach, including details on MD simulations, cases studied and theoretical background of mechanical properties. In section 3, results and discussion will be presented, followed by section 4 containing the conclusions and closing remarks.

2. Numerical approach

2.1. Molecular model

In this study, the ReaxFF force-field was adopted for modeling a-SiO_2 [52, 53]. ReaxFF is a reactive bond-order based force field and is usually derived by fitting against a training set containing both quantum mechanical and experimental data. ReaxFF has been shown to better reproduce the mechanical properties of a-SiO_2 compared to two and three body force-fields [48, 54]. In general, ReaxFF contains ten energy terms:

$$
\begin{aligned}
E_{\text{total}} = {} & E_{\text{bond}} + E_{\text{over}} + E_{\text{under}} + E_{\text{lp}} + E_{\text{val}} \\
& + E_{\text{pen}} + E_{\text{tors}} + E_{\text{conj}} + E_{\text{vdW}} + E_{\text{coul}}.
\end{aligned}
\tag{1}
$$

E_{bond} describes the energy of single, double and triple bonds. E_{over} and E_{under} represents the energy terms due to complex interactions that cause a specific atom type to have over and under coordination with other atom types, respectively. E_{lp}

5

127 accounts for modeling the lone electron pairs. E_{val} is related to the valence angle.
128 E_{pen} considers a penalty coming from cumulative double bonds in a particular va-
129 lency angle. E_{tors} describes all different torsional configurations. E_{conj} represents
130 the conjugated double bonds effect. E_{vdW} considers non-bonded interactions and
131 E_{coul} is the energy contribution due to electrostatic interactions.

2.2. Simulation setup

133   Fig. 1(a) shows a snapshot of a MD simulation of uniaxial tensile loading of
134 a-SiO$_2$. To simplify the analysis, the plane stress conditions are used in the *x-y*
135 plane and periodic boundary conditions are applied in all directions. The dimen-
136 sions of the a-SiO$_2$ sample in three directions are $L_x = 29.41$ nm, $L_y = 29.41$ nm,
137 and $L_z = 1.51$ nm, which are chosen so that the accuracy and computational cost
138 are equally achieved [47]. The sample was made by replicating a smaller model
139 of dimensions $4.91 \times 4.91 \times 1.51$ nm^3 by $6 \times 6 \times 1$ in all three directions. This
140 small a-SiO$_2$ model was created through a melt-and-quench process starting from
141 a β-cristobalite structure. Details about this process, as well as a verification of
142 the amorphous structure were presented in our recent study [47].
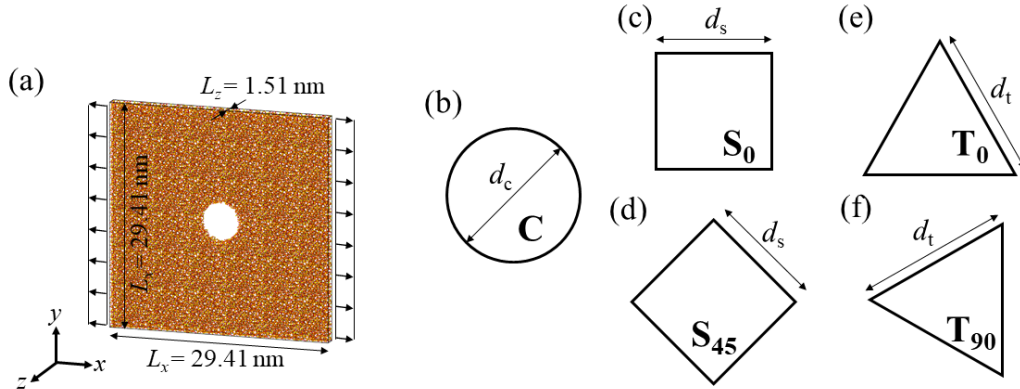
143

Figure 1: (a) A snapshot of a MD simulation of uniaxial tensile loading on amorphous silica with a circular pore. Dimensions of the silica model are also included. (b-f) Various pore structures that are investigated in this study, including (b) A circular pore with a diameter d_c, (c) A square pore with a side length d_s, (d) A square pore with a side length d_s rotated at 45 degrees, (e) An equilateral up-triangular pore with a side length d_t, (f) An equilateral right-triangular pore with a side length d_t. The bold letters denote the abbreviation for each pore structure.

144   In this study, we are interested in nanometer scale pore structures as they have
145 been observed in nanoporous a-SiO$_2$. Fig. 2 shows the SEM and TEM images of

colloidal SiO_2 and Santa Barbara Amorphous-16 (SBA-16), which are among the most popular a-SiO_2 based materials. Colloidal SiO_2 based materials are usually used to prepare photonic and magnetic materials, porous polymer membranes, etc. [55]. SBA-family based materials are mostly known for their textural properties and are widely studied for catalysis, energy materials, and drug delivery [56]. In these porous materials, the pore sizes were measured approximately from 2 to 5 nm.
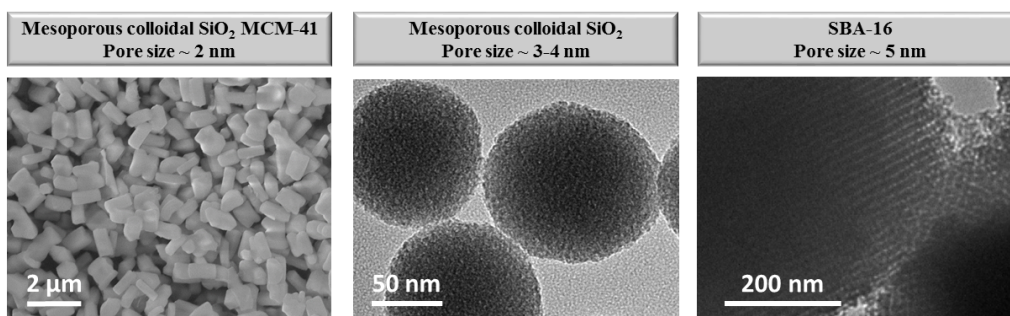

Figure 2: SEM and TEM images of several silica based materials[1]. From left to right, they are mesoporous colloidal SiO_2 MCM-41 (from SEM), mesoporous colloidal SiO_2 (from TEM), and SBA-16 (from TEM).

Inspired by the internal pore structure of silica based materials, in our simulations, we looked at the pore sized ranging from 4.43 to 9.43 nm. Furthermore, the pores are located at the center of the sample. Three pore shapes including circle, square and equilateral triangle[2] are studied. The square and triangle shapes are also rotated to investigate the effect of pore orientation. In total, five pore structures are investigated in this study as shown in Figs. 1(b-f). Therein, "C", "S", and "T" describe the circle, square, and triangle shapes, respectively, while the subscript numbers describe the rotational angle. The diameter of the circle pore is d_c, and the the side length of the square and triangle pores are d_s, and d_t, respectively. To avoid the simulation artifact due to the boundary, the distance from the pore edge to the sample's edge is much larger than the ReaxFF cut-off distance.

---

[2]For convenience, from now, we refer equilateral triangle as triangle.

Therefore, the pore spacing in our simulations might be larger compared to experimental measurements. However, the focus of the present work is on the nanopore structures on mechanical properties of a-SiO$_2$ rather than the pore spacing effect. Three porosity values (ϕ) are considered: 2.27, 3.27, and 4.45%. Table 1 shows the dimensions of the pore structures at various porosity. Moreover, the number of atoms in our simulations varies from 82,560 to 86,400 atoms, which is high compared to recent ReaxFF MD studies on a-SiO$_2$ [44, 45, 48, 49, 50, 51]. Such high number increases computational cost, but guarantees better averaging.

Table 1: Dimensions of nanopore structures used in this study.

Porosity ϕ (%)	d_c (nm)	d_s (nm)	d_t (nm)
2.27	5.00	4.43	6.73
3.27	6.00	5.32	8.08
4.45	7.00	6.20	9.43

To perform the uniaxial tensile loading, the simulation box of a-SiO$_2$ is subjected to a constant displacement rate along the x-direction at each time step. All atoms are forced to deform via an affine transformation that exactly matches the box deformation. It should be noted that only positions are altered due to remapping but the velocities of these atoms remained unchanged. The engineering strain-rate, ε_{xx}, was set to 8×10^9 s^{-1}, which is in the region where Young's modulus is independent from the strain rate [48]. Temperature of 300 K and pressure of 1 atm are maintained throughout the simulation using the NPT (constant number of atoms, pressure, and temperature) ensemble. Before deformation, the system was equilibrated for 100 ps. All the simulations were carried out using LAMMPS [57]. Chenoweth et al. suggested that a time step smaller than 0.5 fs is sufficient for the charges and bond order to change at every time step [58]. In this study, the time step was set to 0.25 fs, which has been used in previous studies on fracture dynamics of a-SiO$_2$ [51, 45, 49, 46, 44].

2.3. Theoretical background

In this paper, we attempt to quantify the effect of pore structures on Young's modulus E and critical energy release rate G_{IC} (the subscript "I" denotes fracture mode I). These mechanical properties are fundamental and are the most used properties in determining the range of usefulness, characterizing mechanical performance, and establishing the service life of materials in the elastic region and

beyond. In addition, G_{IC} has been usually used as the threshold value where the initiated crack starts to propagate in continuum fracture modeling [26, 59, 60, 61].

Young's modulus is determined as the slope of the global stress-strain curve (σ_{xx}-ε_{xx}) up to 5% strain through linear regression. A similar limit was applied in the other papers [47, 48]. Stress components are computed using the classical definition as [62]:

$$\sigma_{kl} = -\frac{1}{V}\left(m\mathbf{v}_k\mathbf{v}_l + \mathbf{F}_{kl}\right).$$

(2)

V is the total volume of the system. The first term on the right hand side is the kinetic component. m is the atomic mass. $\mathbf{v}_k$ and $\mathbf{v}_l$ are the velocity components in the k- and l-directions, respectively. $\mathbf{F}_{kl}$ is the virial component, which describes the intra and intermolecular interactions.

At the beginning of the deformation process, the mechanical energy of the system is zero as the system is free from stress. That energy is stored when the the loading increases; however, a crack does not initiate nor propagate due to insufficient stress intensity. When the loading is large enough, the stored mechanical energy is released during crack propagation. When the sample is completely fractured, the stored mechanical energy drops to zero as the system is once again free from stress. Thus, the critical energy release rate G_{IC} is calculated by integrating the stress-strain curve over the whole process as [63]:

$$G_{IC} = \frac{L_y L_z}{\Delta A} L_x \int_0^{\varepsilon_{xx}^f} \sigma_{xx} d\varepsilon_{xx}.$$

(3)

ΔA is the total area of the new created surface. ε_{xx}^f is strain at the end of the fracture. Surface area was calculated through construction of a surface mesh using OVITO software [64]. A spherical probe molecule with a radius of 4.5 Å and a smoothing level of 10 were used. It should be noted that similar parameters have been applied in previous study [49].

3. Results and Discussion

Fig. 3 shows the uniaxial stress-strain responses that were obtained from all simulations. In each sub-figure, we compare the data of the sample without pore and with various pore structures. Figs. 3(a-c) show the results at different porosity values of 2.27, 3.27, and 4.45%, respectively. In all cases, stress increases linearly

9

until it reaches its ultimate value (σ_{xx}^{u}). Then, stress decreases with increasing strain as crack initiates and propagates. From the stress-strain curves, we are able to calculate Young's modulus (E) and the critical energy release rate (G_{IC}) as discussed in the subsection 2.3.

At first glance, one can observe the significant effect of nanopore on the stress-strain response. The presence of nanopore reduces the slope of the stress-strain curve. This reduction increases with increasing porosity. The results also confirm the effect of nanopore structure (e.g. pore shape and orientation) under a given porosity. Detailed results and discussion are presented in the following subsections.

3.1. Effect of nanopore structure on Young's modulus

3.1.1. Young's modulus and porosity

Fig. 4 shows Young's modulus as a function of porosity. Each data point is an average of five values derived from five porous sample associated with a corresponding porosity. As expected, Young's modulus decreases with an increase in porosity. Young's modulus of the sample without any pore is 72.83 GPa, which shows an excellent agreement with experimental results [65, 66]. Based on the data obtained from our MD simulations, we found that Young's modulus of porous a-SiO$_2$ decreases exponentially with an increase in porosity. This exponential trend has also been observed in other porous materials [67, 68]. However, the effect of nanopores under the same porosity remains unknown. To address this, we quantify the effect of pore structure on Young's modulus using potential energy.

3.1.2. Impact of pore morphology on Young's modulus

a-SiO$_2$ is mainly classified as a brittle material and, thus exhibits Hookean behavior. For such a material, elastic energy is stored when the object undergoes deformation, and is released when the force is removed and the object returns to original shape. This elastic energy is a form of potential energy, as it is stored in the bonds between atoms in an object when it is temporarily under stress. Thus, we hypothesize that potential energy per atom (PE/atom) can be used to quantify the effect of pore structure on Young's modulus. Fig. 5 presents the variation of Young's modulus with the average PE/atom, which was calculated when the system was deformed at 5% strain.
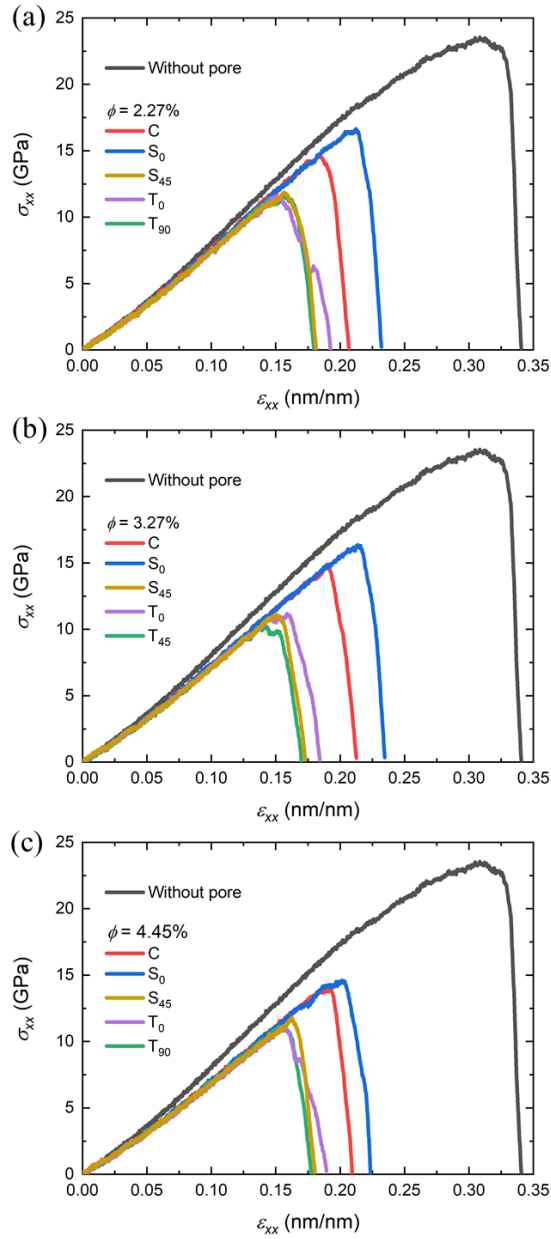
Figure 3: Stress-strain curves obtained from all simulations at various porosity values: (a) $\phi = 2.27\%$, (b) $\phi = 3.27\%$, and (c) $\phi = 4.45\%$. For each porosity, five different nanopore structures were studied. In each sub-figure, the data for the case without any pore was also presented.
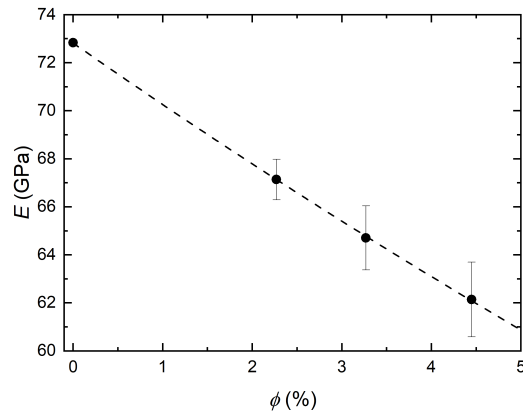
11

Figure 4: Dependence of porosity ϕ on Young's modulus E. The error bars reflect the average of the samples with different pore structures but with the same porosity. The dashed line reflects the fitting curve.
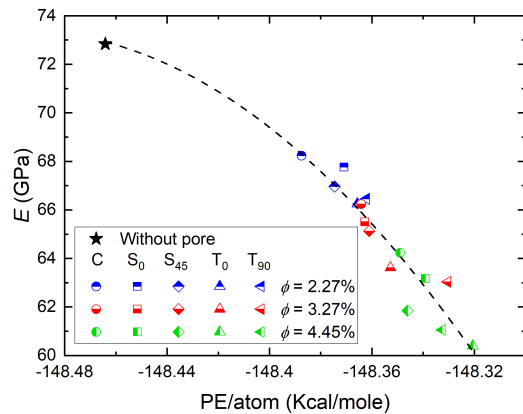
Figure 5: Young's modulus E as a function of average PE/atom which was calculated when the system was deformed at 5% strain. The legends describe the color coding for pore structure and porosity. The dashed lines are the polynomial fitting to the data.

The results in Fig. 5 clearly demonstrated the dependence of Young's modulus on pore structure and porosity. In addition to highlighting the Young's modulus dependency on porosity, Fig. 5 also highlights Young's modulus increases with a reduction in the amount of PE/atom. Notes that potential energy is a negative value, thus a smaller value implies a stronger attractive energy. In another word, as one expected, this result indicates that an increase in intermolecular interaction energy improves Young's modulus as an indication of enhanced stiffness.

The variation of PE/atom with pore structures highlights the influence of the scale effect. The presence of nanopore induces a free surface where surface atoms have fewer interatomic bonds compared to bulk. The lack of these interactions influences the bond length and binding energy of surface atoms, leading to different behavior from the atom in bulk. Even though the porosity values are quite low in this study (less than 4.5%), due to a large surface-to-volume ratio at the nanoscale, surface atoms have a significant impact on the mechanical properties of the material.

Fig. 6 illustrates the potential energy distribution around the nanopores for cases with 2.27% porosity at the equilibrium stage. Similar distributions were also found in cases with higher porosity. The potential energy distribution was shown in a blue-green-red color scale, where red denotes the atoms with a higher energy (a weaker binding energy) and blue indicates the opposite. One can observe a distinguish region around the pore due to the free surface effect.
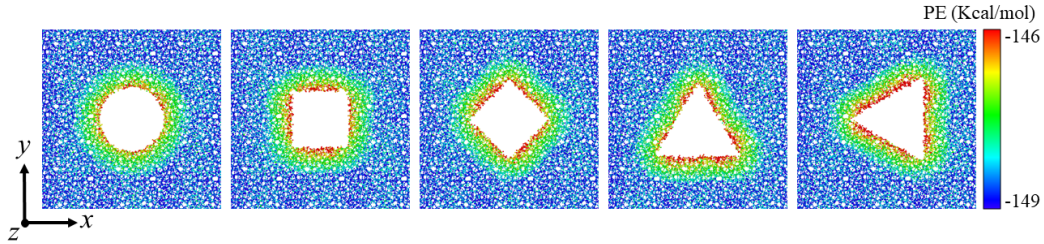

Figure 6: Potential energy distribution around the nanopore at the equilibrium stage (0% strain). The visualizations shown here are from the cases with a porosity of 2.27%. From left to right, the data was obtained for C, S_0, S_{45}, T_0, and T_{90} samples.

The results show more red atoms around the triangular pore than the square and circular ones. This observation was also confirmed by the data in Fig. 5 where circular pore case has a smaller PE/atom (stronger interaction energy) than square and triangular pore cases. This is due to a broader distribution of potential energy in the circular pore case, which leads to a reduction of the surface tension. A wider distribution of potential energy enables more efficient bond creation, leading to an increase in the coordination number. Whereas, the presence of the atoms in the edges, facet, steps, and corners leads to an odd distribution of the coordination number that coexists among them. The bonds cannot rearrange to a lower energy configuration because of the gap in the distribution in the coordination

13

number. Also, the triangular pore shape with three corners has higher potential energy with respect to the square shape with four corners. This is because of each edge of the triangle shape carries more potential energy to distribute along the total surface.

From the obtained results and the investigation of the nanopore structures in this study, we can infer that pore shape has a strong effect on Young's modulus. A circular pore leads to the highest Young's modulus, followed by the square pore and the triangular pore with the lowest. However, it seems that pore orientation has a less significant impact on Young's modulus.

Fig. 5 shows inconsistent variation between Young's modulus and pore orientation for all porosity values. For example, considering the triangular pore cases at 2.27 and 4.45% porosity, Young modulus of the T_{90} sample is larger than the corresponding one of the T_0 sample. However, that trend does not hold for 3.27% porosity. This can be explained by the aspect ratio (r_a) of the pore geometry. Torres-Sanchez et al. [17] observed the dependence of stiffness of porous Ti35Nb4Sn on aspect ratio of pore ranging from 0 to 40. However, in this study, for both the S_0 and S_{45} samples, the aspect ration remains the same ($r_a = 1$). For the T_0 and T_{90} samples, this ratio changes a bit, from 1.15 to 0.87, respectively. This change is considered relatively small. Thus, in this study, the aspect ration as an indicator of the pore geometry cannot be used to explain the effect of pore orientation.

3.2. Effect of nanopore structure on critical energy release rate

3.2.1. Energy release rate and porosity

Following the above subsection examining the effect of pore structure on Young's modulus was discussed, this subsection investigates the role of pore structure on critical energy release rate. We first propose a ligament length to quantify the pore structural feature as a mean to investigate pore morphology impact on energy release rate.

The impact of porosity on G_{IC} is shown in Fig. 7, where each G_{IC} data point is an average of five G_{IC} values derived from five porous sample associated with corresponding porosity. G_{IC} of the sample without any pore is 18.86 J/m^2, which is comparable to the other studies [44, 69]. Although our simulation results show that G_{IC} drops significantly with the presence of nanopore, it slightly decreases
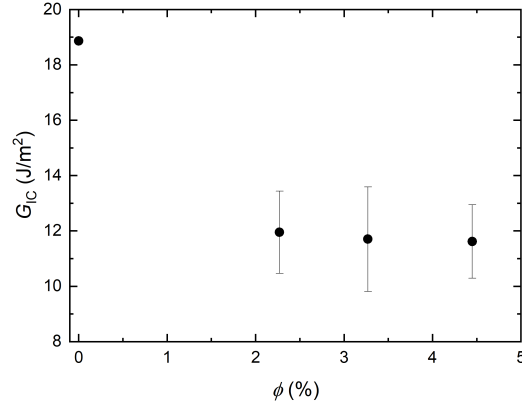
14

Figure 7: Variation of critical energy release rate G_{IC} with porosity ϕ. The error bars reflect the average of the samples with different pore structures but the same porosity.

3.2.2. Crack in tensile loading and pore ligament

Crack pattern is always of interest as it is a signature of a fracture event. Considering the scenario in this study as shown in Fig. 1, the crack path is usually formed along the central line perpendicular to the loading direction. This phenomenon has been observed a lot in the literature [51, 70, 63, 71]. Even though the existing of voids might alter the propagation path, we expect that the overall pattern will not to be affected significantly. To justify that, we will show stress distribution and crack pattern in the following.

Brittle materials do not undergo significant plastic deformation. Their failure is caused by breaking of the bonds between atoms, which usually requires a tensile stress along the bond. The bond breakage is aided by the presence of defect which induces tensile stress concentration. Additionally, despite the fact that the von Mises stress (VMS) originates from the macroscopic distortion energy criterion, it has been recently applied at nanoscale to explain the material deformation as well as crack growth [72, 73, 74], which is directly related to the motion of a dislocation. Therefore, we show in Fig. 8(a) and Fig. 8(b) tensile stress (σ_{xx}) and VMS (σ_{vm}) distributions for cases with 2.27% porosity, respectively. It should be noted that similar distributions were also found in the cases with higher porosity. The data in Fig. 8 was obtained at 10% strain and was not normalized by the
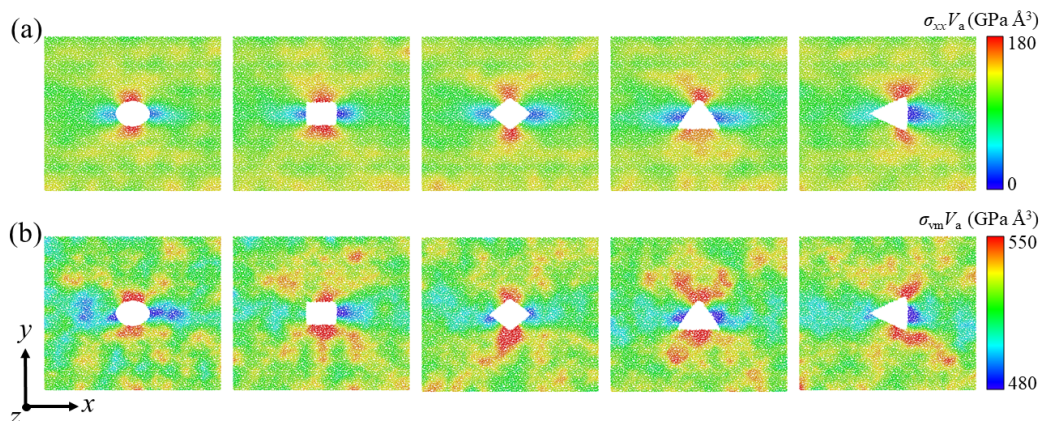
15

atomic volume.

Figure 8: (a) Tensile stress σ_{xx} and (b) von Mises stress σ_{vm} distributions of the samples with 2.27% porosity at 10% strain. From left to right, the data was obtained for C, S_0, S_{45}, T_0, and T_{90} samples, respectively. The data has not been normalized by the atomic volume (V_a).

In Fig 8, regardless of the pore shape and orientation, high stress concentration occurs at the top and bottom of the pore, implying the locations of the crack initiation. We also observe that the high stress gradient is perpendicular to the loading direction (x-direction), while the low stress gradient is along the loading directions. According to Eq. 2, stress includes two components, the kinetic and virial components. The former one is due to temperature, which is maintained at 300 K during the deformation. Thus, the kinetic term does not play a significant role in the variation of stress. Meanwhile, the virial term is due to molecular forces, which is mainly caused by density. A higher density leads to a higher molecular forces due to more interactions between atoms. Thus, in order to understand the stress distributions in Fig 8, we need to observe the displacement of atoms during the tensile deformation.

Fig. 9 show the displacement vectors of all atoms from two points of the system: 0% and 10% strain. These results are based on porosity value of 2.27%. Similar vector contours were also observed in the other samples with higher porosity. It should be noted that the displacement vectors in Fig. 9 contain only the internal (non-affine) displacements of the particles. Meanwhile, the contributions to the particle displacements that stem from the macroscopic deformation of the simulation cell were filtered out. The results agree with the stress distributions shown in

Fig. 8. Particularly, majority of the displacement happens around the nanopores. Therein, the atoms tend to displace and concentrate at the top and bottom of the pore, leading to high stress concentration. Meanwhile, on both sides of the pore in the loading direction (i.e. x-direction), the atoms tend to move away from the pore edge, causing low density and thus low stress.
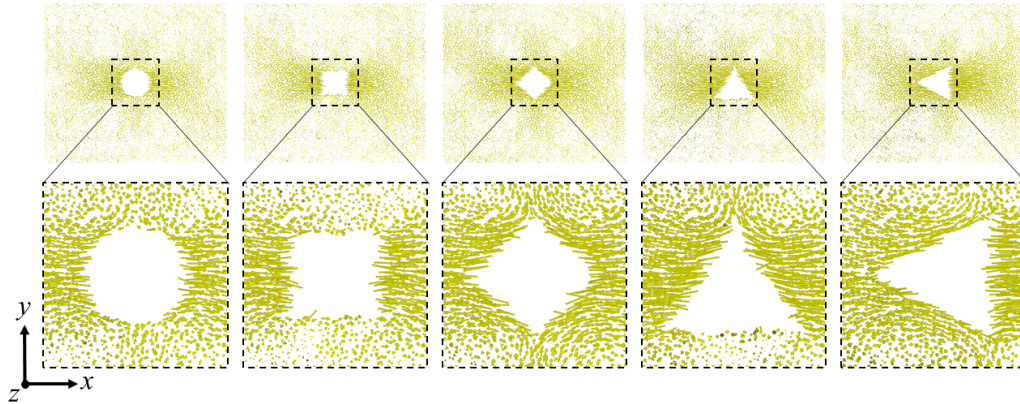

Figure 9: Displacement vectors of atoms from two points of the systems of 2.27% porosity: 0% and 10% strain. The result for all atoms were shown in the top row, while a close-up view of the pores are shown in the bottom. For a better view, only a thin layer of 0.4 nm thickness in the z-direction was shown. From left to right, the data was obtained for C, S_0, S_{45}, T_0, and T_{90} samples.

The stress distribution (in Fig. 8) and displacement vectors (in Fig. 9) suggest that the crack will initiate and propagate along the central line in the y-direction, which is consistent with fracture pattern in macro scale as discussed above. To confirm this, Fig. 10 shows the crack pattern associated with all of our cases at 2.27% porosity. The green surface represents the isolated surface including both pore and fractured surfaces. Ignoring the subtle variations, the crack patterns are similar regardless of the pore structure. Similar results were observed in the other cases with higher porosity.

Eq. 3 suggests that fractured surface is a critical factor determining the surface energy that dissipates during fracture propagation. In particular, energy release rate is the integral of strain energy along the fracture surface from $\varepsilon_{xx} = 0$ to $\varepsilon_{xx} = \varepsilon_{xx}^{f}$. Assuming that the variation in the thickness of the samples (in the z-direction) is negligible, the fracture path from the pore edge to sample edge is
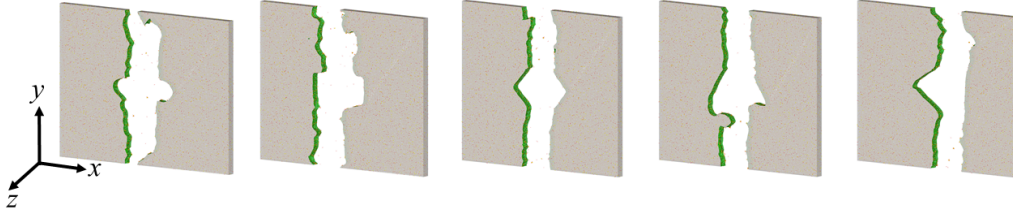
17

Figure 10: Fracture pattern of the samples with a porosity of 2.27%. The gray surface denotes the periodic surface, while the green surface represents the isolated surface. From left to right, the data was obtained from the C, S_0, S_{45}, T_0, and T_{90} samples.

closely related to G_{IC}. One can conclude that a longer path may lead to a larger fracture strain (ε_{xx}^f) and, thus, a higher fracture energy release. It is noteworthy that different pore structures (e.g., shape, orientation, etc.) lead to different fracture path length. Thus, to distinguish the fracture path lengths, ligament length can be used to quantify the pore structure effect on the energy release rate. Ligament length is defined as the shortest distance from the pore edge to the sample edge, which is usually referred as an average pore wall thickness by experimentalists [75, 76]. Fig. 11 illustrates the ligament length (L_{lig}) for our selective nanopore structures.
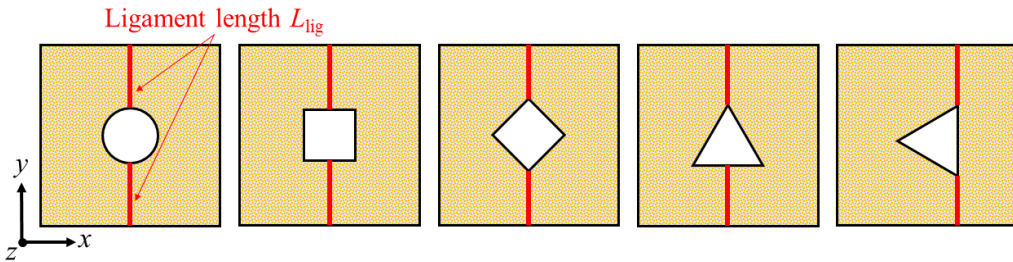

Figure 11: Definition of the ligament length L_{lig} with various pore structure with the loading condition applied in this study.

3.2.3. Impact of pore morphology on energy release rate

Fig. 12 shows how the critical energy release rate varies as a function of ligament length in different cases. The results confirm our hypothesis that an increase in ligament length would increase the energy release rate.

As discussed above, the integral in Eq. 3, which is the area of the region bounded by the stress-strain curve, solely determines the critical energy release
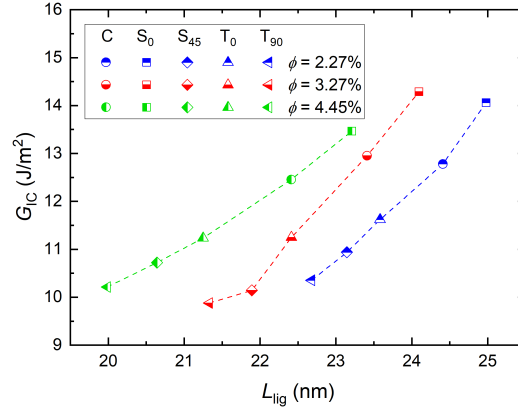
18

Figure 12: Variation of critical energy release rate G_{IC} with ligament length L_{lig} at various porosity.

rate. As shown in Fig. 3, for a given porosity, the dependence of the slope of the stress-strain curves on nanopore structure is relatively small. As a result, the energy release rate is significantly affected by the fracture strain (ε_{xx}^f) in a proportional fashion. Fig. 13 shows the dependence of fracture strain on ligament length, which follows the similar trend as energy release rate (as shown in Fig. 12). The results confirmed that the critical energy release rate is proportional to the fracture strain. Furthermore, such dependencies indicate that ligament length is a viable parameter in characterizing the effect of pore structure on fracture properties in porous media.

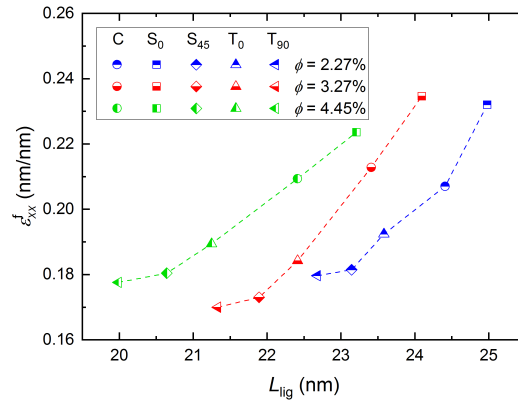Figure 13: Variation of fracture strain ε_{xx}^f with ligament length L_{lig} at various porosity.

3.3. Applications and scale-up

From the results given above, we believe that with further investigation, we can quantify fracture mechanism of more complex single-pore structures in terms of ligament thickness.

The results in our study suggested that the critical energy release rate can be manipulated. In general, an increase in porosity reduces the energy release rate. However, this trend is impacted the underlying pore structures. As shown in Figs. 12 and 13, the energy release rate can be maintained or even increased with an increase in porosity if ligament length is unchanged or reduced, respectively. With recent development in nano-technologies, controlling ligament length of porous materials is possible [19, 77, 78, 79, 80]. It allows to manufacture porous materials with controllable pore morphology for desirable macroscopic performances.

Moreover, the results in the present work are applicable to cases with different pore sizes but similar porosity values. As one could expect, for the same of similar porosity values, both Young's modulus and critical energy release rate should be smaller when the pore size is smaller. These expectations have been confirmed through a simulation with a smaller circular pore (3.33 nm). In this case, porosity of 2.27% remained the same as the original circular case with pore size of 5.00 nm. Details of these two cases are presented in Table 2. The results indicate that the relationship between PE/atom and Young's modulus, as well as ligament length and critical energy release rate can be generalized to other cases beyond what has been presented in this work. However, further systematic studies are necessary when the pore shape and orientations are varied [40].

Table 2: Comparison between two cases with the same pore shapes and porosity but different pore sizes. In both cases, $L_x = L_y$ and $L_z = 1.5$ (nm).

Case	ϕ (%)	L_x (nm)	d_c (nm)	L_{lig} (nm)	E (GPa)	$G_{\mathbf{IC}}$ (J/m^2)
1	2.27	29.41	5.00	24.41	68.23	13.68
2	2.27	19.61	3.33	16.28	68.15	12.54

4. Conclusions

In this paper, the effect of nanopore structure including pore shape and orientation on mechanical properties of a-SiO$_2$ (Young's modulus and critical energy

release rate) was studied using MD simulations. In addition to different pore structures, various porosity values were also considered. Based on the results, the main findings are summarized as follows:

- The presence of nanopores strongly affects the mechanical properties of the material. Young's modulus of a-SiO$_2$ decreases as an exponential function with respect to porosity. Energy release rate of a-SiO$_2$ decreases significantly with the presence of nanopore. However, the variation in change of the energy release rate is not noticeable when porosity changes.

- The effect of nanopore structure on Young's modulus can be quantified using PE/atom. Young's modulus is enhanced with improving intermolecular interaction energy. Pore orientation has a mild effect on Young's modulus. In contrast, changing pore shape varies the surface tension and thus, affects Young's modulus more profoundly. A circular pore leads to the highest Young's modulus, followed by the square and triangular pores.

- Ligament length, which is defined as the shortest distance from the pore edge to the sample edge, can be used to characterize the effect of pore structure on critical energy release rate. A longer ligament length implies a longer fracture path and, thus, a higher surface energy that dissipates during fracture propagation.

- The dependency of Young's modulus and critical energy release rate on geometrical features proposed in this study can be applied to other cases with similar porosity values.

Based on the findings in this study, mechanical properties of nanoporous materials with more complex pore structures can be predicted. In addition, the results suggested that the desired properties can be archived by nano-engineering pore structures in porous materials. Finally, the results in this study can be implemented to continuum models to investigate the fracture mechanisms of porous a-SiO$_2$.

Data availability

The raw/processed data required to reproduce these findings cannot be shared at this time as the data also forms part of an ongoing study.

Declaration of Competing Interest

The authors declare that they have no known competing financial interests or personal relationships that could have appeared to influence the work reported in this paper.

Author Contribution

Truong Vo: Conceptualization, Methodology, Investigation, Software, Formal analysis, Validation, Visualization, Writing - original draft, Writing - review & editing. **Bang He**: Conceptualization, Investigation, Writing - original draft, Writing - review & editing. **Michael Blum**: Software, Writing - review & editing. **Angelo Damone**: Investigation, Writing - review & editing. **Pania Newell**: Conceptualization, Funding acquisition, Supervision, Project administration, Writing - review & editing.

Acknowledgements

References

[1] B.-L. Su, C. Sanchez, X.-Y. Yang, Hierarchically structured porous materials: from nanoscience to catalysis, separation, optics, energy, and life science, John Wiley & Sons, 2012.

[2] H. Yamada, K. Tamura, Y. Watanabe, N. Iyi, K. Morimoto, Geomaterials: their application to environmental remediation, Science and technology of advanced materials 12 (2011) 064705.

22

[3] K. Mediaswanti, C. Wen, E. Ivanova, C. Berndt, F. Malherbe, V. Pham, J. Wang, A review on bioactive porous metallic biomaterials, J Biomim Biomater Tissue Eng 18 (2013) 2–8.

[4] W. Li, K. Lu, J. Walz, Freeze casting of porous materials: review of critical factors in microstructure evolution, International materials reviews 57 (2012) 37–60.

[5] R. L. Vekariya, A. Dhar, P. K. Paul, S. Roy, An overview of engineered porous material for energy applications: a mini-review, Ionics 24 (2018) 1–17.

[6] L. Yuan, S. Ding, C. Wen, Additive manufacturing technology for porous metal implant applications and triple minimal surface structures: A review, Bioactive Materials 4 (2019) 56–70.

[7] H. Cho, M. H. Bartl, M. Deo, Bubble point measurements of hydrocarbon mixtures in mesoporous media, Energy & Fuels 31 (2017) 3436–3444.

[8] S. Rashidi, J. A. Esfahani, A. Rashidi, A review on the applications of porous materials in solar energy systems, Renewable and Sustainable Energy Reviews 73 (2017) 1198–1210.

[9] J. Delgado, et al., Industrial and technological applications of transport in porous materials, Springer, 2013.

[10] D. S. Smith, A. Alzina, J. Bourret, B. Nait-Ali, F. Pennec, N. Tessier-Doyen, K. Otsu, H. Matsubara, P. Elser, U. T. Gonzenbach, Thermal conductivity of porous materials, Journal of Materials Research 28 (2013) 2260–2272.

[11] H. Li, S. M. Oppenheimer, S. I. Stupp, D. C. Dunand, L. C. Brinson, Effects of pore morphology and bone ingrowth on mechanical properties of microporous titanium as an orthopaedic implant material, Materials Transactions 45 (2004) 1124–1131.

[12] L. J. Pyrak-Nolte, D. J. DePaolo, T. Pietraß, Controlling subsurface fractures and fluid flow: a basic research agenda, Technical Report, USDOE Office of Science (SC)(United States), 2015.

[13] M. Tirrell, S. Hubbard, D. Sholl, Basic Research Needs for Energy and Water, Technical Report. Office of Science, Technical Report, U.S. Department of Energy, 2017.

[14] R. de Borst, Computational Methods for Fracture in Porous Media: Isogeometric and Extended Finite Element Methods, Elsevier, 2017.

[15] O. Coussy, Poromechanics, John Wiley & Sons, 2004.

[16] X. Lu, M. Viljanen, Fibrous insulation materials in building engineering applications, in: Fibrous and Composite Materials for Civil Engineering Applications, Elsevier, 2011, pp. 271–305.

[17] C. Torres-Sanchez, J. McLaughlin, R. Bonallo, Effect of pore size, morphology and orientation on the bulk stiffness of a porous ti35nb4sn alloy, Journal of Materials Engineering and Performance 27 (2018) 2899–2909.

[18] J. Biener, A. M. Hodge, J. R. Hayes, C. A. Volkert, L. A. Zepeda-Ruiz, A. V. Hamza, F. F. Abraham, Size effects on the mechanical behavior of nanoporous au, Nano letters 6 (2006) 2379–2382.

[19] M. K. Khristosov, S. Dishon, I. Noi, A. Katsman, B. Pokroy, Pore and ligament size control, thermal stability and mechanical properties of nanoporous single crystals of gold, Nanoscale 9 (2017) 14458–14466.

[20] A. Mathur, J. Erlebacher, Size dependence of effective young's modulus of nanoporous gold, Applied physics letters 90 (2007) 061910.

[21] T. Dutta, S. Tarafdar, Fractal pore structure of sedimentary rocks: Simulation by ballistic deposition, Journal of Geophysical Research: Solid Earth 108 (2003).

[22] S. Ozaki, Y. Aoki, T. Osada, K. Takeo, W. Nakao, Finite element analysis of fracture statistics of ceramics: Effects of grain size and pore size distributions, Journal of the American Ceramic Society 101 (2018) 3191–3204.

[23] A. Abdulle, A. Nonnenmacher, A short and versatile finite element multiscale code for homogenization problems, Computer Methods in Applied Mechanics and Engineering 198 (2009) 2839–2859.

[24] L. Simoni, B. A. Schrefler, Multi field simulation of fracture, in: Advances in Applied Mechanics, volume 47, Elsevier, 2014, pp. 367–519.

[25] R. de Borst, Chapter 1 - introduction, in: R. de Borst (Ed.), Computational Methods for Fracture in Porous Media, Elsevier, 2018, pp. 1 – 12. URL: http://www.sciencedirect.

24

573   com/science/article/pii/B9780081009178000010.   doi:https:
574   //doi.org/10.1016/B978-0-08-100917-8.00001-0.

[26] B. He, L. Schuler, P. Newell, A numerical-homogenization based phase-field fracture modeling of linear elastic heterogeneous porous media, Computational Materials Science 176 (2020) 109519.

[27] A. Ural, S. Mischinski, Multiscale modeling of bone fracture using cohesive finite elements, Engineering Fracture Mechanics 103 (2013) 141–152.

[28] C. V. Verhoosel, J. J. Remmers, M. A. Gutiérrez, R. De Borst, Computational homogenization for adhesive and cohesive failure in quasi-brittle solids, International Journal for Numerical Methods in Engineering 83 (2010) 1155–1179.

[29] S. P. Patil, Y. Heider, C. A. H. Padilla, E. R. Cruz-Chú, B. Markert, A comparative molecular dynamics-phase-field modeling approach to brittle fracture, Computer Methods in Applied Mechanics and Engineering 312 (2016) 117–129.

[30] A. C. Hansen-Dörr, L. Wilkens, A. Croy, A. Dianat, G. Cuniberti, M. Kästner, Combined molecular dynamics and phase-field modelling of crack propagation in defective graphene, Computational Materials Science 163 (2019) 117–126.

[31] P. Chakraborty, Y. Zhang, M. R. Tonks, Multi-scale modeling of microstructure dependent intergranular brittle fracture using a quantitative phase-field based method, Computational Materials Science 113 (2016) 38–52.

[32] A. Liu, Q. Peng, A molecular dynamics study of the mechanical properties of twisted bilayer graphene, Micromachines 9 (2018) 440.

[33] C. T. Nguyen, M. Barisik, B. Kim, Wetting of chemically heterogeneous striped surfaces: Molecular dynamics simulations, AIP Advances 8 (2018) 065003.

[34] T. Q. Vo, B. Kim, A molecular dynamics study on cooling rate effect on atomic structure of solidified silver nanoparticles, The European Physical Journal D 73 (2019) 183.

[35] T. Q. Vo, M. Barisik, B. Kim, Near-surface viscosity effects on capillary rise of water in nanotubes, Physical Review E 92 (2015) 053009.

[36] S. P. Patil, Y. Heider, A review on brittle fracture nanomechanics by all-atom simulations, Nanomaterials 9 (2019) 1050.

[37] E. Bitzek, J. R. Kermode, P. Gumbsch, Atomistic aspects of fracture, International Journal of Fracture 191 (2015) 13–30.

[38] A. Taloni, M. Vodret, G. Costantini, S. Zapperi, Size effects on the fracture of microscale and nanoscale materials, Nature Reviews Materials 3 (2018) 211.

[39] N. V. Priezjev, M. A. Makeev, Evolution of the pore size distribution in sheared binary glasses, Physical Review E 96 (2017) 053004.

[40] N. Winter, M. Becton, L. Zhang, X. Wang, Effects of pore design on mechanical properties of nanoporous silicon, Acta Materialia 124 (2017) 127–136.

[41] D. Şopu, C. Soyarslan, B. Sarac, S. Bargmann, M. Stoica, J. Eckert, Structure-property relationships in nanoporous metallic glasses, Acta materialia 106 (2016) 199–207.

[42] L. Giraldo, B. López, L. Pérez, S. Urrego, L. Sierra, M. Mesa, Mesoporous silica applications, in: Macromolecular symposia, volume 258, Wiley Online Library, 2007, pp. 129–141.

[43] I. I. Slowing, B. G. Trewyn, S. Giri, V.-Y. Lin, Mesoporous silica nanoparticles for drug delivery and biosensing applications, Advanced Functional Materials 17 (2007) 1225–1236.

[44] S. C. Chowdhury, E. A. Wise, R. Ganesh, J. W. Gillespie Jr, Effects of surface crack on the mechanical properties of silica: A molecular dynamics simulation study, Engineering Fracture Mechanics 207 (2019) 99–108.

[45] J. M. Rimsza, R. E. Jones, L. J. Criscenti, Crack propagation in silica from reactive classical molecular dynamics simulations, Journal of the American Ceramic Society 101 (2018) 1488–1499.

[46] T. Hao, Z. M. Hossain, Atomistic mechanisms of crack nucleation and propagation in amorphous silica, Physical Review B 100 (2019) 014204.

[47] T. Vo, B. Reeder, A. Damone, P. Newell, Effect of domain size, boundary, and loading conditions on mechanical properties of amorphous silica: A reactive molecular dynamics study, Nanomaterials 10 (2020) 54.

[48] S. C. Chowdhury, B. Z. G. Haque, J. W. Gillespie, Molecular dynamics simulations of the structure and mechanical properties of silica glass using reaxff, Journal of Materials Science 51 (2016) 10139–10159.

[49] J. M. Rimsza, R. E. Jones, L. J. Criscenti, Chemical effects on subcritical fracture in silica from molecular dynamics simulations, Journal of Geophysical Research: Solid Earth 123 (2018) 9341–9354.

[50] J. M. Rimsza, R. Jones, L. Criscenti, Mechanisms of silica fracture in aqueous electrolyte solutions, Frontiers in Materials 6 (2019) 79.

[51] H. Mei, Y. Yang, A. C. van Duin, S. B. Sinnott, J. C. Mauro, L. Liu, Z. Fu, Effects of water on the mechanical properties of silica glass using molecular dynamics, Acta Materialia 178 (2019) 36–44.

[52] A. C. Van Duin, S. Dasgupta, F. Lorant, W. A. Goddard, Reaxff: a reactive force field for hydrocarbons, The Journal of Physical Chemistry A 105 (2001) 9396–9409.

[53] J. C. Fogarty, H. M. Aktulga, A. Y. Grama, A. C. Van Duin, S. A. Pandit, A reactive molecular dynamics simulation of the silica-water interface, The Journal of chemical physics 132 (2010) 174704.

[54] Y. Yu, B. Wang, M. Wang, G. Sant, M. Bauchy, Revisiting silica with reaxff: towards improved predictions of glass structure and properties via reactive molecular dynamics, Journal of Non-Crystalline Solids 443 (2016) 148–154.

[55] A. Galukhin, D. Bolmatenkov, A. Emelianova, I. Zharov, G. Y. Gor, Porous structure of silica colloidal crystals, Langmuir 35 (2019) 2230–2235.

[56] V. Valtchev, S. Mintova, M. Tsapatsis, Ordered porous solids: recent advances and prospects, Elsevier, 2011.

[57] S. Plimpton, Fast parallel algorithms for short-range molecular dynamics, Journal of computational physics 117 (1995) 1–19.

27

[58] K. Chenoweth, A. C. Van Duin, W. A. Goddard, Reaxff reactive force field for molecular dynamics simulations of hydrocarbon oxidation, The Journal of Physical Chemistry A 112 (2008) 1040–1053.

[59] B. He, P. Newell, Multi-physics modeling of injected nanoparticles effect on remediation of co2 leakage through cracks, International Journal of Greenhouse Gas Control 95 (2020) 102955.

[60] X. Zhang, S. W. Sloan, C. Vignes, D. Sheng, A modification of the phase-field model for mixed mode crack propagation in rock-like materials, Computer Methods in Applied Mechanics and Engineering 322 (2017) 123–136.

[61] C. Miehe, S. Mauthe, Phase field modeling of fracture in multi-physics problems. part iii. crack driving forces in hydro-poro-elasticity and hydraulic fracturing of fluid-saturated porous media, Computer Methods in Applied Mechanics and Engineering 304 (2016) 619–655.

[62] D. Tsai, The virial theorem and stress calculation in molecular dynamics, The Journal of Chemical Physics 70 (1979) 1375–1382.

[63] L. Brochard, G. Hantal, H. Laubie, F. J. Ulm, R. J.-M. Pellenq, Fracture mechanisms in organic-rich shales: role of kerogen, in: Poromechanics V: proceedings of the fifth Biot conference on poromechanics, 2013, pp. 2471–2480.

[64] A. Stukowski, Visualization and analysis of atomistic simulation data with ovito–the open visualization tool, Modelling and Simulation in Materials Science and Engineering 18 (2009) 015012.

[65] S. M. Wiederhorn, Fracture surface energy of glass, Journal of the American Ceramic Society 52 (1969) 99–105.

[66] N. P. Bansal, R. H. Doremus, Handbook of glass properties, Elsevier, 2013.

[67] R. R. Reddy, O. Prakash, P. V. Reddy, The effect of porosity on elastic moduli of yba2cu3o7-δ high tc superconductors, Applied superconductivity 3 (1995) 215–222.

[68] Z. Chen, X. Wang, V. Bhakhri, F. Giuliani, A. Atkinson, Nanoindentation of porous bulk and thin films of la0. 6sr0. 4co0. 2fe0. 8o3-δ, Acta Materialia 61 (2013) 5720–5734.

[69] O. Rodriguez, A. Matinmanesh, S. Phull, E. H. Schemitsch, P. Zalzal, O. M. Clarkin, M. Papini, M. R. Towler, Silica-based and borate-based, titania-containing bioactive coatings characterization: critical strain energy release rate, residual stresses, hardness, and thermal expansion, Journal of functional biomaterials 7 (2016) 32.

[70] M. Bauchy, H. Laubie, M. A. Qomi, C. Hoover, F.-J. Ulm, R.-M. Pellenq, Fracture toughness of calcium–silicate–hydrate from molecular dynamics simulations, Journal of Non-Crystalline Solids 419 (2015) 58–64.

[71] Y. Zhang, P. C. Millett, M. R. Tonks, X.-M. Bai, S. B. Biner, Molecular dynamics simulations of intergranular fracture in uo2 with nine empirical interatomic potentials, Journal of Nuclear Materials 452 (2014) 296–303.

[72] T. Tang, S. Kim, J. Jordon, M. Horstemeyer, P. T. Wang, Atomistic simulations of fatigue crack growth and the associated fatigue crack tip stress evolution in magnesium single crystals, Computational materials science 50 (2011) 2977–2986.

[73] H. Dai, G. Chen, S. Li, Q. Fang, B. Hu, Influence of laser nanostructured diamond tools on the cutting behavior of silicon by molecular dynamics simulation, RSC advances 7 (2017) 15596–15612.

[74] S. Xu, X. Deng, Nanoscale void nucleation and growth and crack tip stress evolution ahead of a growing crack in a single crystal, Nanotechnology 19 (2008) 115705.

[75] N. Badwe, X. Chen, K. Sieradzki, Mechanical properties of nanoporous gold in tension, Acta Materialia 129 (2017) 251–258.

[76] I. McCue, J. Stuckner, M. Murayama, M. J. Demkowicz, Gaining new insights into nanoporous gold by mining and analysis of published images, Scientific reports 8 (2018) 1–11.

[77] D. Mo, J. Liu, J. Duan, H. Yao, H. Latif, D. Cao, Y. Chen, S. Zhang, P. Zhai, J. Liu, Fabrication of different pore shapes by multi-step etching technique in ion-irradiated pet membranes, Nuclear Instruments and Methods in Physics Research Section B: Beam Interactions with Materials and Atoms 333 (2014) 58–63.

29

[78] H.-J. Qiu, J. Kang, P. Liu, A. Hirata, T. Fujita, M. Chen, Fabrication of large-scale nanoporous nickel with a tunable pore size for energy storage, Journal of Power Sources 247 (2014) 896–905.

[79] L. M. Rueschhoff, L. A. Baldwin, R. Wheeler, M. J. Dalton, H. Koerner, J. D. Berrigan, N. M. Bedford, S. Seifert, M. K. Cinibulk, M. B. Dickerson, Fabricating ceramic nanostructures with ductile-like compression behavior via rapid self-assembly of block copolymer and preceramic polymer blends, ACS Applied Nano Materials 2 (2018) 250–257.

[80] X. Zheng, Z. Fu, K. Du, C. Wang, Y. Yi, Minimal surface designs for porous materials: from microstructures to mechanical properties, Journal of Materials Science 53 (2018) 10194–10208.